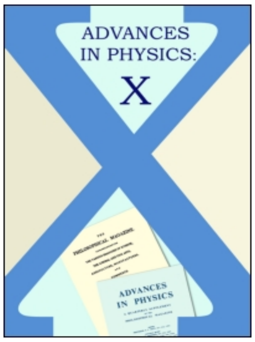

Advances in Physics: X

ISSN: (Print) 2374-6149 (Online) Journal homepage: http://www.tandfonline.com/loi/tapx20

Brillouin scattering of phonons in complex materials

Carlo E. Bottani & Daniele Fioretto

To cite this article: Carlo E. Bottani & Daniele Fioretto (2018) Brillouin scattering of phonons in complex materials, Advances in Physics: X, 3:1, 1467281, DOI: 10.1080/23746149.2018.1467281

To link to this article: https://doi.org/10.1080/23746149.2018.1467281

ADVANCES IN PHYSICS: X, 2018
VOL. 3, NO. 1, 1467281
https://doi.org/10.1080/23746149.2018.1467281

Taylor & Francis
Taylor & Francis Group

REVIEW ARTICLE

Brillouin scattering of phonons in complex materials

Carlo E. Bottani[a] and Daniele Fioretto[b]

[a]Dipartimento di Energia, Politecnico di Milano via Ponzio, Italy; [b]Dipartimento di Fisica e Geologia, Università degli Studi di Perugia Via Alessandro Pascoli, Italy

ABSTRACT
Initially, the theory of propagation of long-wavelength acoustic phonons and Brillouin scattering of laser light in condensed matter is concisely summarized. Then, the case of two relevant classes of complex materials in which Brillouin scattering can be measured is reviewed. First, in *low-density, low-dimensional, disordered materials*, the crossover between confinement and propagation is discussed on the basis of experimental findings. Moreover, the possibility of measuring the *local* mechanical properties of these materials at the mesoscale by Brillouin scattering is critically discussed. Second the application of Brillouin scattering to biological materials, a rather hot topic, is presented.

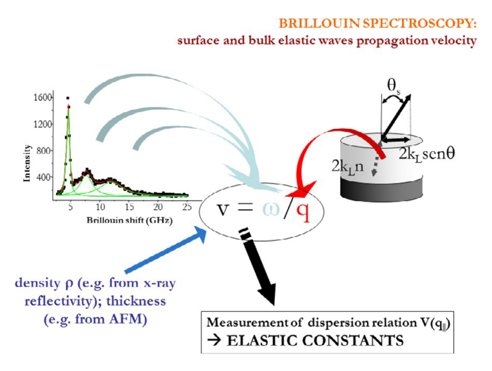

ARTICLE HISTORY
Received 13 March 2018
Accepted 15 April 2018

KEYWORDS
Brillouin scattering; nanomaterials; biomaterials; cluster-assembled materials

PACS CODES
78.35.+c Brillouin scattering, condensed matter; 81.05.U- Carbon-based materials; 81.07.-b Nanoscale materials and structures: fabrication and characterization; 87.80. Dj Biophysical techniques (research methods). Spectroscopies

The acoustic waves and their phonons

Though the traditional ways to measure the mechanical properties of materials and, in particular, the elastic constants, are based on quasi-static deformation processes (e.g. the tensile test to measure the Young modulus), many important methods are acoustic in nature or make use of acoustic phenomena (ultrasound

CONTACT Carlo E. Bottani carlo.bottani@polimi.it

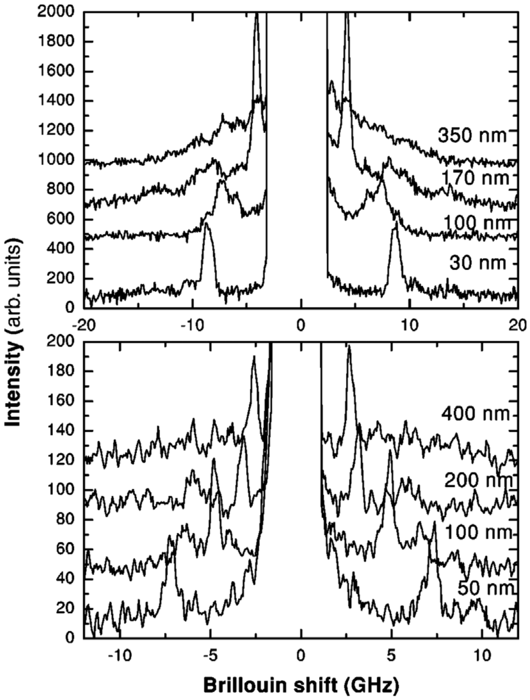

Figure 1. (Top) Brillouin spectra from films of different thickness, deposited using unfocused beams (larger clusters). In these measurements, the incidence angle is 50°. The effect of varying the thickness is reflected in the intensity of the modes (Rayleigh and Sezawa) traveling in the film and in their velocity. (Bottom) Brillouin spectra from films deposited using a focused beam (smaller clusters) and having different thicknesses. The figure is taken from ref. [29].

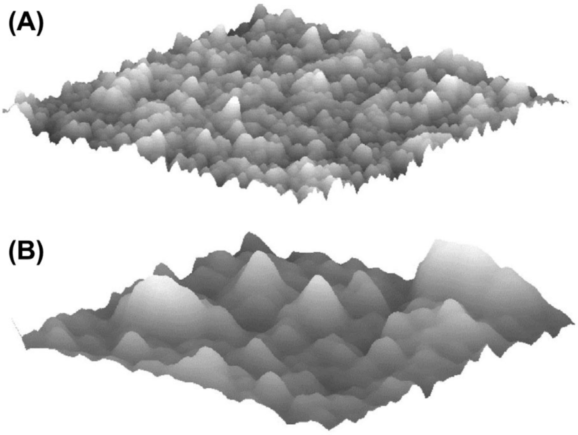

Figure 2. Atomic force microscopy pictures of the surface topography of two nano-structured carbon films assembled with small clusters (A) and with large clusters (B). The figure is taken from ref. [29].

propagation, acoustic microscopy, acoustic emission, Brillouin scattering, laser-induced surface acoustic waves) [1,2]. To face the less naive methods and more complex geometries/structures (low-dimensional and nano-structured materials

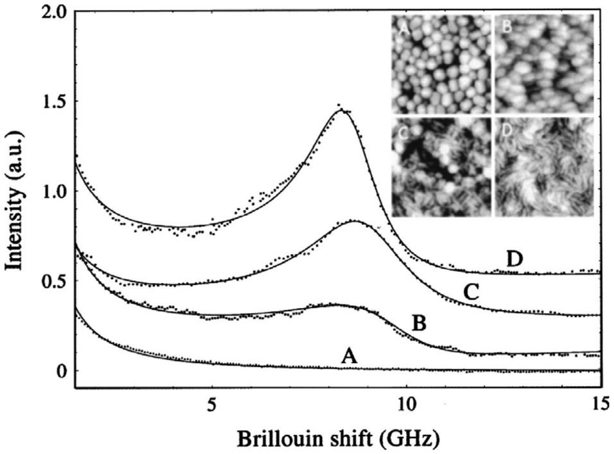

Figure 3. Brillouin spectra (anti-Stokes branch) of PTFE films: non-sintered film (a) and films sintered at 331 °C for approximately 130 s (b), 300 s (c), and 3 h (d). Full lines represent fits to the experimental data. Inset: AFM images describe the corresponding surface structural evolution through the sintering process. Reproduced from ref. [31], with permission of AIP publishing https://doi.org/10.1063/1.1558972.

[17]), some basic results of both classical elastodynamics [3,4] and quantum lattice dynamics have to be employed.

Recently, Brillouin scattering of LASER light from acoustic waves has been used to characterize also biological materials, a quite hot and relevant topic for both basic and medical applications.

Bulk waves

For the sake of simplicity, we consider here as reference the case of ideal isotropic and continuous materials The fundamental elastodynamic (wave) equation describing long-wavelength acoustic lattice waves could be either derived as a vanishing wavevector limit from microscopic lattice dynamics of crystals or, phenomenologically, directly stated from continuous mechanics, without assuming any microscopic periodicity, in terms of the dynamic elastic displacement field $\mathbf{u} = \mathbf{u}(\mathbf{r},\ t)$ and reads:

$$\frac{\partial^2 \mathbf{u}}{\partial t^2} = v_t^2 \nabla^2 \mathbf{u} + (v_l^2 - v_t^2) \boldsymbol{\nabla}(\boldsymbol{\nabla} \cdot \mathbf{u}) \tag{1}$$

where $v_l = \sqrt{\left(B + \frac{4}{3}\mu\right)/\rho}$ is the longitudinal sound velocity and $v_t = \sqrt{\mu/\rho}$ is the transverse sound velocity. Here, ρ is the mass density, B the bulk modulus, and μ the shear modulus. Remembering that the most general deformation process is the superposition of a simple dilation and of a simple shear, a solution of the type $\mathbf{u} = \mathbf{u}_l + \mathbf{u}_t$, with $\boldsymbol{\nabla} \times \mathbf{u}_l = 0$ and $\boldsymbol{\nabla} \cdot \mathbf{u}_t = 0$, can be always be written (Kirchhoff

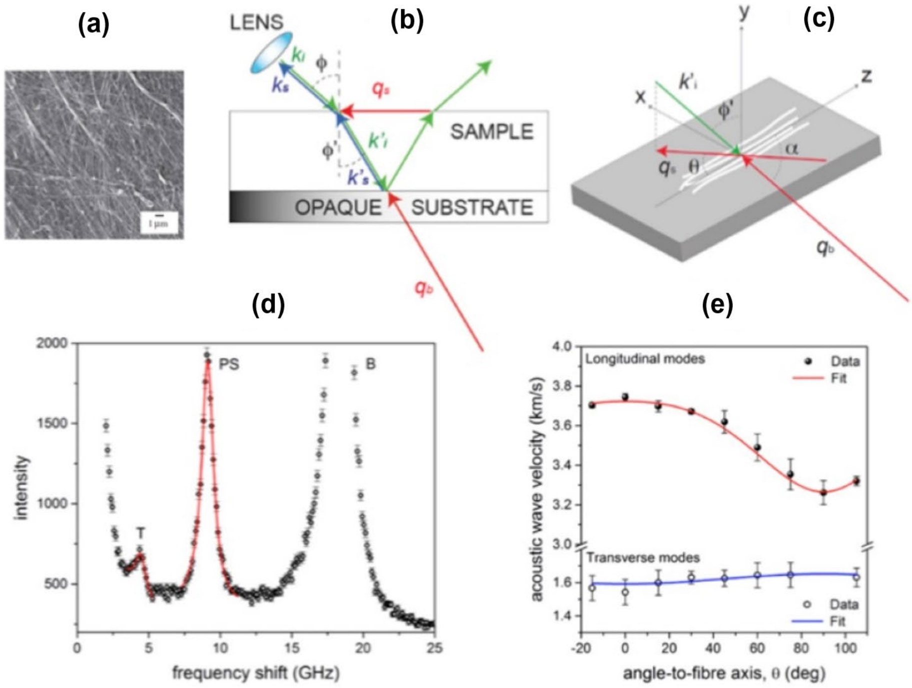

Figure 4. (a) Scanning electron micrograph of a type I collagen fiber from rat tail tendon, acquired after the BLS measurement. (b) Schematic diagram of the BLS scattering geometry using a specimen in contact with the surface of a reflective silicon substrate. The incident light (k_i) passes through the lens, is refracted at the air–sample interface (k_{0i}) and focused at the sample–substrate interface. The scattered light collected by the same lens (k_{0s}) results from interaction with both bulk phonons (q_b) and those traveling PS of the sample (q_s). Angles between the directions of light and the normal to the surface are indicated as φ and φ_0. (c) Schematic diagram of the sample and of the adopted coordinate system; z defines the extraordinary axis parallel to the direction of the fibers. Angles θ and α are those between the direction of phonons q_s and q_b to the z-axis, respectively. k_i, k_{0i}, k_s, k_{0s}: wavenumbers of the incident and scattered light; q_b, q_s, wavevectors of the bulk and PS modes, respectively. (d) Brillouin spectrum obtained at $\theta = 30°$. Labels T, PS, and B denote peaks related to transverse, parallel-to-surface and bulk modes, respectively. (e) Plot of the longitudinal and transvers acoustic wave velocities vs angle to fiber axis, obtained from PS and T Brillouin peaks. Reprinted from refs. [37] and [41].

theorem). The second condition is identical to that holding for electromagnetic waves in vacuum. This method perfectly works (even though anisotropic materials, crystals, require a more complex treatment [2]) leading to two decoupled simple *wave equations* for $\mathbf{u}_l$ and $\mathbf{u}_t$:

$$\frac{\partial^2 \mathbf{u}_l}{\partial t^2} = v_l^2 \nabla^2 \mathbf{u}_l \quad \text{and} \quad \frac{\partial^2 \mathbf{u}_t}{\partial t^2} = v_t^2 \nabla^2 \mathbf{u}_t \tag{2}$$

The fundamental bulk solution of Equation (1) is then the superposition of three independent monochromatic plane waves, one longitudinal (LA) and two (mutually perpendicular) transverse (TA_1, TA_2), of the type:

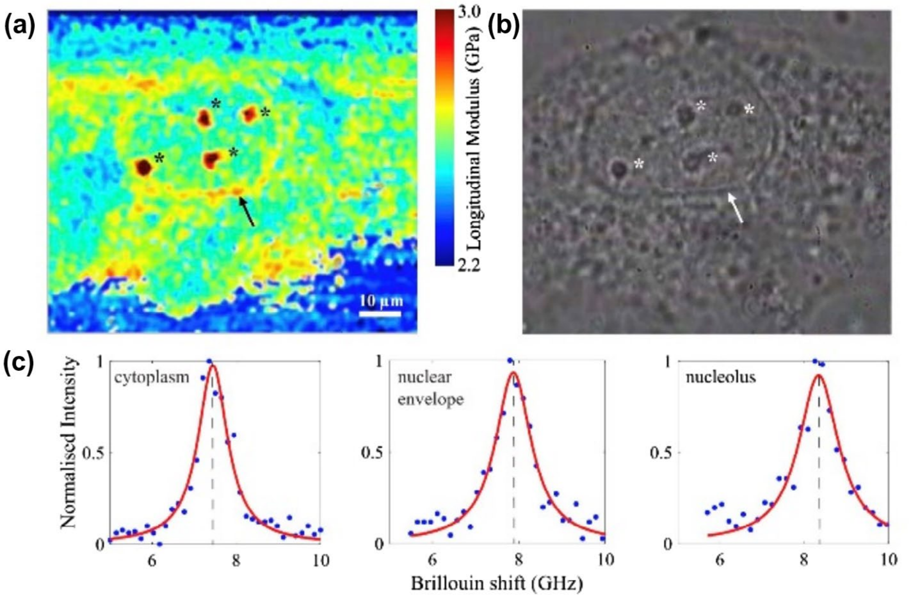

Figure 5. High-resolution Brillouin image of a single cell *in vitro*. A cross section through a single-cultured human umbilical vein endothelial cell imaged using both Brillouin (a) and phase contrast (b) microscopy at 100x magnification. Reprinted from ref. [39].

$$\mathbf{u}_\alpha = \Re\left\{ Q_{\mathbf{q}\alpha}\mathbf{e}_{\mathbf{q}\alpha}e^{i[\mathbf{q}\cdot\mathbf{r}-\omega_\alpha(\mathbf{q})t)]} \right\} \tag{3}$$

where $\mathbf{q}$ is the wavevector, α is a branch index ($\alpha = l, t_1, t_2$), $Q_{\mathbf{q}\alpha}$ is the complex amplitude of the *normal coordinate* $\xi_\alpha(\mathbf{q}) = Q_{\mathbf{q}\alpha}e^{-i\omega t}$ and $\mathbf{e}_{\mathbf{q}\alpha}$ a *polarization unit vector* ($\mathbf{e}_{\mathbf{q}l}||\mathbf{q}$; $\mathbf{e}_{\mathbf{q}t}\perp\mathbf{q}$). Moreover, $\omega_l(\mathbf{q}) = v_l|\mathbf{q}|$ and $\omega_{t_1,t_2}(\mathbf{q}) = v_t|\mathbf{q}|$, for in the isotropic case the circular frequency ω does not depend on the direction of wavector $\mathbf{q}$.

Time dependence: anelastic relaxation

In Equation (1), through the sound speeds, the adiabatic elastic constants B and μ appear [3]. Real deformation processes are irreversible and time dependence should be introduced in the stress–strain relationship. In terms of frequency one should be capable of treating both very slow phenomena (almost zero frequency), like the creep of a viscoelastic polymeric material under constant stress, and extremely fast ones like the propagation of an acoustic wave in a diamond crystal at more than 200 GHz. The simple description in terms of viscosity used for fluids is almost never a good approximation for solids. The simplest phenomenological way to treat anelastic damping and sound absorption in solids is the so-called Zener's standard model [5]. A more refined theory can be found in [6,7]. Confining ourselves to the uniaxial stress case, the model generalizes Hooke's law as follows:

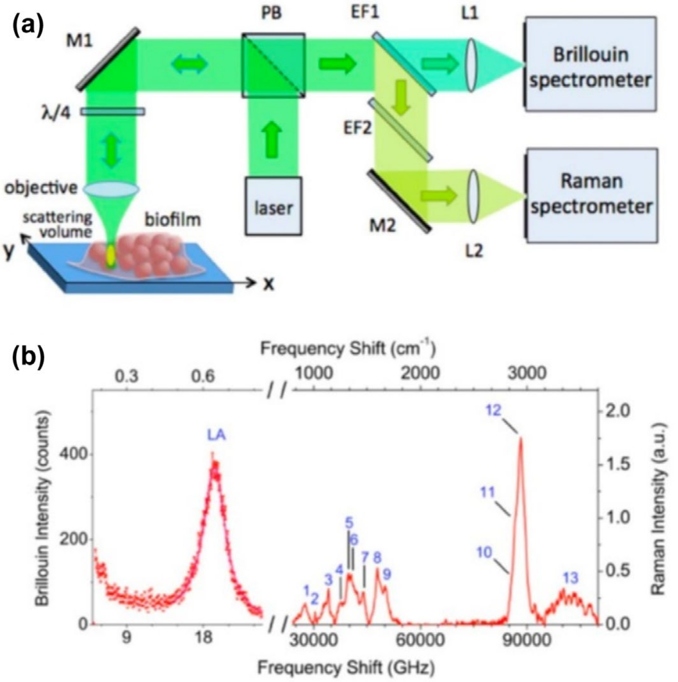

Figure 6. Schematic of the Brillouin–Raman micro-spectroscopy instrument. Light from a single-mode laser source is focused onto the sample by the same objective that is also used to collect the back-scattered light. The sample is mounted onto a piezo translation stage for mapping measurements. A polarizing beam splitter (PB) transmits the depolarized backscattered light to the spectrometers. Immediately after, a short-pass tunable edge filter (EF1) transmits the quasielastic scattered light to a Brillouin spectrometer, made by a new concept of tandem Fabry–Perot interferometer, and reflects the deeply inelastic scattered light into a single-stage Raman spectrometer. More details on the setup and on the attribution of the peaks in Brillouin and Raman spectra recorded from Candida biofilms can be found in ref. [57] and [59].

$$\sigma + \tau_{\varepsilon}\frac{d\sigma}{dt} = E_R\left(\varepsilon + \tau_{\sigma}\frac{d\varepsilon}{dt}\right) \tag{4}$$

When the strain ε is kept constant, the stress σ relaxes exponentially with a relaxation time τ_ε. Conversely, τ_σ is the strain relaxation time when the stress is kept constant. E_R is the value of the pertinent elastic modulus after all relaxation has occurred (*relaxed* elastic modulus): it corresponds to the thermodynamic equilibrium value E of classical elasticity. In view of the application of Equation (4) to periodic wave phenomena, neglecting for the moment space dispersion (wavevector dependence), periodic dynamical stresses and strains are assumed $\sigma(t) = \sigma_o e^{i\omega t}$ and $\varepsilon(t) = \varepsilon_o e^{i\omega t}$. Then, Equation (4) becomes:

$$\left(1 + i\omega\tau_{\varepsilon}\right)\sigma_o = E_R\left(1 + i\omega\tau_{\sigma}\right)\varepsilon_o \tag{5}$$

In this way, Hooke's law is restored introducing a frequency-dependent complex elastic modulus $\tilde{E}(\omega) = \sigma_o/\varepsilon_o$:

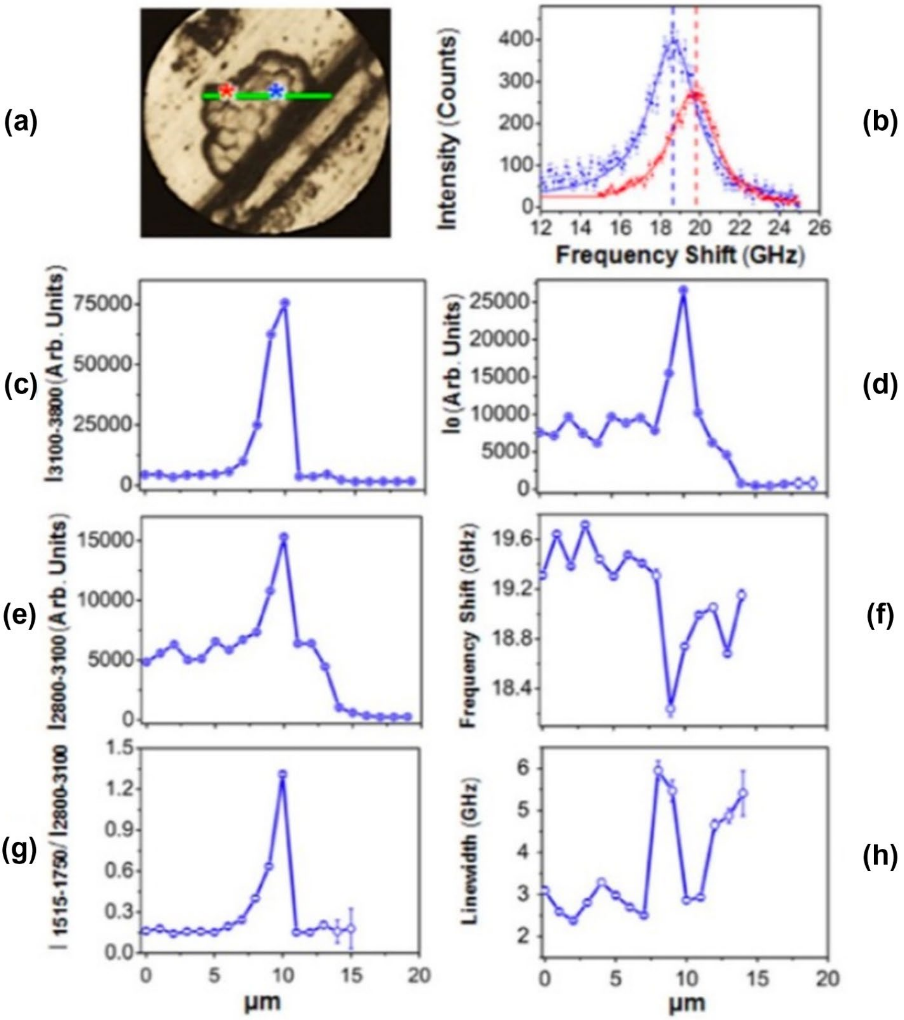

Figure 7. Photomicrograph and analysis of Brillouin and Raman spectra of a *C. albicans* biofilm. (a) Optical image of the biofilm. The green line, 20-μm long, is where Brillouin and Raman spectra were collected with 1 μm steps; (b) Brillouin spectra (dots) from the locations indicated with asterisks in (a), together with the DHO (Equation 7) fitting curves (full lines). (d) Brillouin intensity I0, (f) frequency shift and (h) linewidth, obtained with the DHO fitting function. (c) Raman integrated intensity of the OH (water) region (3100–3800 cm^{-1}), (e) CH region (2800–3100 cm^{-1}), and (g) ratio between the integrated intensity of the Amide I+EPS constituents + Cytochrome C and the CH_2 and CH_3 stretching regions. See ref. [59].

$$\begin{aligned} \tilde{E}(\omega) &= E'(\omega) + iE''(\omega) \\ E'(\omega) &= E_R \frac{1+\omega^2\tau_\varepsilon\tau_\sigma}{1+(\omega\tau_\varepsilon)^2} = E_U + \frac{(E_R - E_U)}{1+(\omega\tau_\varepsilon)^2} \\ E''(\omega) &= E_R \frac{\left(\tau_\varepsilon - \tau_\sigma\right)\omega}{1+(\omega\tau_\varepsilon)^2} = \frac{(E_U - E_R)\omega\tau_\varepsilon}{1+(\omega\tau_\varepsilon)^2} \end{aligned} \tag{6}$$

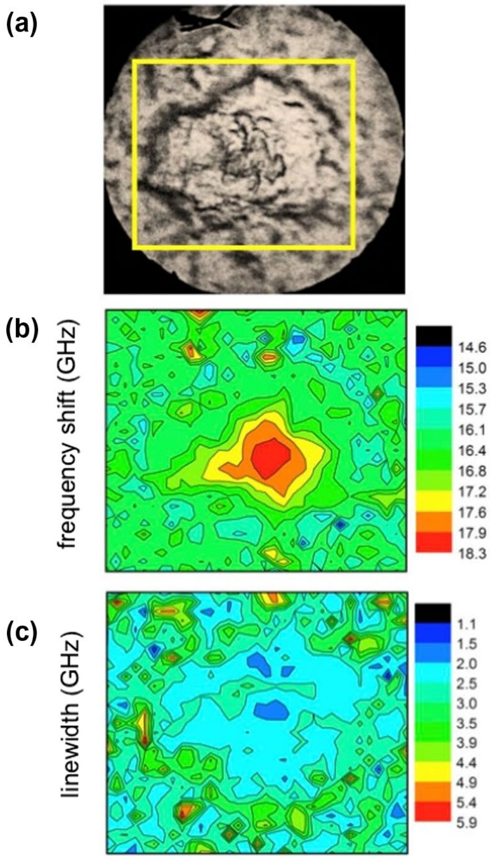

Figure 8. (a) Photomicrograph of a mouse brain hippocampal section containing a single plaque collected with the Brillouin microscope. Yellow box denotes a 60 × 60 μm^2 area, where a Brillouin map was acquired using a 1.5-μm step-size. Maps based on the (b) frequency shift and (c) linewidth of the Brillouin peaks. See ref. [64].

At zero frequency, $\tilde{E}(0) = E_R$ and σ_o is in phase with ε_o. At high frequency, when $\omega\tau_\varepsilon >> 1$, $\tilde{E}(\infty) = E_R\left(\tau_\sigma/\tau_\varepsilon\right) = E_U$ is the so-called *unrelaxed* elastic modulus. Defining the dissipation or *internal friction* Q^{-1} as the fraction of energy lost per radian of vibration, when dissipation is small one obtains:

$$Q^{-1} \approx \frac{E''(\omega)}{E'(\omega)} = \Delta_E \frac{\omega\tau}{1 + (\omega\tau)^2} \tag{7}$$

where $\tau = \sqrt{\tau_\varepsilon \tau_\sigma}$ and $\Delta_E = \left(E_U - E_R\right)/\sqrt{E_U E_R}$ is the *relaxation strength* of the modulus. In thermoelasticity, where the only accounted dissipation process is heat diffusion, $E_U = E_S = \left(\partial^2 F/\partial\varepsilon^2\right)_S > E_R = E_T$, E_S being the *adiabatic modulus* and $E_T = E = \left(\partial^2 F/\partial\varepsilon^2\right)_T$ is the *isothermal modulus*. Thus, in thermoelastic wave propagation at high frequency [3] it is sufficient substituting the isothermal elastic constants with the (slightly higher) adiabatic ones. The above treatment strictly follows Debye's theory of dispersion of the dielectric constant in insulating materials and the dissipation peak in the frequency dependence of Q^{-1} is called a Debye peak. Despite the naive approach, Debye peaks are quite ubiquitous and can describe several dissipation processes [5].

Equation (4) is just a very particular and trivial form of a much general linear stress–strain relation which takes into account the presence of several dissipation mechanisms including the case of a continuous spectrum of relaxation times. Respecting the causality principle and assuming time-invariance, this relation can be written as:

$$\sigma(t) = E_U \varepsilon(t) + \int_0^\infty h_E(\xi)\varepsilon(t-\xi)d\xi \tag{8}$$

The complex elastic modulus $\tilde{E}(\omega)$ is then the Fourier transform of $h_E(\xi)$:

$$\tilde{E}(\omega) = E_U + \int_0^\infty h_E(\xi)e^{i\omega\xi}d\xi \tag{9}$$

The Zener model is the case of a single exponential decay for the response function $h_E(t)$. To include the more complex scenario of a distribution of exponential decays, without loss of generality $h_E(\xi)$ can be modeled as a functional of the *relaxation times spectrum* $g_E(\tau)$ as:

$$h_E(\xi) = \int_0^\infty g_E(\tau)e^{-\xi/\tau}d\tau. \tag{10}$$

Phonons

If we neglect damping, the above classical description can be translated into the language of quantum mechanics (see, e.g. [8]) of a system of independent harmonic oscillators $\xi_{\boldsymbol{\alpha}}(\mathbf{q})$ whose quanta are the acoustic phonons[1] with energies:

$$E_n(\mathbf{q}\boldsymbol{\alpha}) = \left(n_{\mathbf{q}\alpha} + \frac{1}{2}\right)\hbar\omega_\alpha(\mathbf{q}) \tag{11}$$

with $n_{\mathbf{q}\alpha} = 0, 1, 2, 3, \ldots$ If the system is in thermodynamic equilibrium at temperature T, the mean values of $n_{\mathbf{q}\alpha}$ are given by the Bose–Einstein factor

$$\langle n_{\mathbf{q}\alpha} \rangle = \frac{1}{e^{\frac{\hbar\omega_\alpha(\mathbf{q})}{k_B T}} - 1} \tag{12}$$

whose high temperature ($k_B T/\hbar\omega_\alpha(\mathbf{q}) >> 1$) classical limit is $k_B T/\hbar\omega_\alpha(\mathbf{q})$. At the end damping can be included again adding an imaginary part to $\hbar\omega_\alpha(\mathbf{q})$ so describing a finite phonon lifetime.

Surface waves

The prototypes of surface acoustic waves (SAWs) are Rayleigh waves. For a treatment of Rayleigh waves see e.g. [3] When the medium is semi-infinite (let us assume the $z = 0$ plane is the *surface*, the medium is below it: $z < 0$) the translational symmetry connected with the plane waves of Equation (3) is broken in the direction perpendicular to the surface. This produces new facts: (a) the reflection of bulk phonons (in general with branch conversion) and (b) the existence of surface waves[3,4]. The simplest case of type (a) is that of a transverse (*TA*) bulk phonon propagating in the *sagittal* (xz) plane with wavevector $\mathbf{q} = q_{||}\hat{\mathbf{e}}_x + q_{\perp}\hat{\mathbf{e}}_z$ polarized in the horizontal y direction (a *shear horizontal* phonon: SH) and impinging on the surface. If the surface is not subjected to external forces, applying the corresponding boundary conditions, one finds that the surface acts as a perfect acoustic mirror and that the *parallel wavevector* $q_{||}$ of the reflected phonon is identical to that of the incident phonon. But, from the dispersion relation for TA phonons, we get

$$q_{\perp} = \sqrt{\frac{\omega^2}{v_t^2} - q_{||}^2}.$$

That is, once $q_{||}$ is fixed, e.g. by the momentum conservation in a light scattering experiment, there is a lower frequency threshold $\omega_t = v_t q_{||}$ for the detectability of SH bulk phonons. Above this frequency, the wave spectrum is *continuous*. If the incident phonon is either a longitudinal or a transverse one but polarized in the incidence plane (*shear vertical*, *SV*), there is both a longitudinal and a transverse phonon reflected at different angles; the *parallel wavevector* $q_{||}$ is always conserved in the reflection. For the longitudinal components to be a true bulk phonons the threshold is $\omega_l = v_l q_{||} > \omega_{t.}$ Otherwise, the corresponding *partial wave* is *evanescent* in nature. The region of the continuous spectrum between ω_t and ω_l is that of the *mixed modes*. What does happen in the spectral region $\omega < \omega_t$ when the polarizations are only *L* and *SV*(*sagittal waves*)? For a given $q_{||}$ there exists a unique *surface wave (*the *Rayleigh wave)*. In other words, there exists also a *discrete spectrum* with a single eigenvalue $\omega_R = v_R q_{||}$. Putting $\omega_R = \xi v_t q_{||}$, v_R is found taking the sole real root of an algebraic sixth-order equation in ξ (see, e.g. [3]) resulting from the insertion of a linear combination of partial waves (one *L* and one *SV*) of the type

$$\boldsymbol{\psi}_{\alpha}(z|\omega_R, q_{||}) = Q_{\mathbf{q}\boldsymbol{\alpha}}\mathbf{e}_{\mathbf{q}\alpha}\exp(-\kappa_{\alpha}z)\exp[iq_{||}(x - v_R t)] \tag{13}$$

in Equation (1) and applying the free surface boundary conditions. Considering the possible values of the Poisson's ratio v, numerical computation shows that ξ can vary between 0.874 and 0.955 and that a good approximation is

$$v_R \simeq \frac{0.862 + 1.14v}{1 + v} v_t$$

Both the *SV* and the *L* components of a Rayleigh wave are non dispersive waves traveling parallel to the surface. Both waves decay exponentially with depth as $\exp(-\kappa_\alpha z)$ with $\kappa_t = q_{||}\sqrt{1-\frac{v_R^2}{v_t^2}}$ and $\kappa_l = q_{||}\sqrt{1-\frac{v_R^2}{v_l^2}}$ showing that the *penetration depth* $\delta_\alpha = \kappa_\alpha^{-1}$ is of the order of the wavelength $\lambda = 2\pi/q_{||}$. This result, together with the existence of the transverse threshold, separating the discrete from the continuous spectrum, is a general feature of surface waves physics even in the presence of overlayers or of a more complex layered subsurface structure. In the general case the transverse threshold depends on the transverse sound velocity of the substrate material.

Complex layered subsurface structures: more general surface waves

Many complex materials can be considered as surface multilayers with, in general, smooth interlayer regions. The most compact way to face the case of such a layered subsurface structure is followed generalizing the treatment of the previous paragraph to an elastic half space ($z \le 0$) whose density ρ and elastic constants B and μ are functions of the depth z. Rigorously, this method would imply to derive again the propagation equation which would take a form different from Equation (1) [9–12]. To our limited purposes one can just think of the same Equation (1) but with z-dependent coefficients. Excluding the case of very sharp interfaces between adjacent layers, this is also a tenable and useful approximation. For the alternative, standard approach, see for example, [13].

Once we have found the surface waves spectrum of a layered structure by means of any numeric methods, a very useful set of spectral functions can be constructed: the layer projected phonon densities of states LPPDS. For given $q_{||}$ and polarization α considering the whole set of eigenfunctions of Equation (1) in the form

$$\phi_{n\alpha}(z|\omega_{n\alpha}, q_{||})\exp[iq_{||}x - \omega_{n\alpha}(q_{||})t]$$

the spectral functions are defined as

$$g_\alpha(\omega, q_{||}|z) = \sum_n < |\phi_{n\alpha}(z|\omega_{n\alpha}, q_{||})|^2 >_{th} \delta(\omega - \omega_{n\alpha}(q_{||})) \tag{14}$$

where $<\ldots>_{th}$ is the thermal average and the summation is over the entire spectrum thought as discrete. The continuous part of the spectrum can be made discrete using a *slab approximation* [9]. In a layered surface structure the Rayleigh wave is not the only true surface wave corresponding to a unique discrete eigenvalue and other surface waves, more or less confined in single or multiple layers, corresponding to several $\omega_{n\alpha}(q_{||})$, can exist (Sezawa, Stoneley and Love waves[13]). The contour lines of a smoothed version of a specific $g_\alpha(\omega, q_{|||}|z)$ in the ω, z plane give a vivid and direct image of phonon localization [14]. The function $g_\alpha(\omega, q_{||}|0)$

is the *surface projected phonon density of states* which plays a major role in surface Brillouin scattering from opaque materials [14].

Brillouin scattering of laser light

Brillouin scattering of laser light is the inelastic coherent scattering of a photon of a monochromatic laser beam propagating in a material from an acoustic phonon. If the acoustic phonons are localized in nanoparticles with size $\delta < \lambda = 2\pi/|\mathbf{k}^I|$, λ being the photon wavelength, then the scattering from an ensemble of independent separated nanoparticles is incoherent and it is better called low-frequency Raman scattering. To save space, the reader is referred to [15] for a detailed description of the experimental setup.

Volume Brillouin scattering

The scattering kinematics can be described in a quite direct and intuitive picture. For the sake of simplicity, we consider both the incident $(\mathbf{k}^I, \omega^I)$ and the scattered $(\mathbf{k}^S, \omega^S)$ photons only *inside* the medium. While a single acoustic phonon $(\mathbf{q}, \omega_\alpha = v_\alpha|\mathbf{q}|)$ is propagating within the material its periodic strain field sets up an anisotropic modulation of the otherwise isotropic dielectric susceptibility χ (Equation 17). This *adiabatic* modulation is viewed as a traveling diffraction grating by the incident electromagnetic wave. Then the scattering kinematics can be explained by the familiar wave concepts of *Bragg reflection* and *Doppler shift*. Equivalently, in the quantum language, the scattering process must obey the laws of conservation of momentum (wavevector) and energy. In the transition from the initial photon state $(\mathbf{k}^I, \omega^I)$ to the final (scattered) photon state $(\mathbf{k}^S, \omega^S)$:

$$\mathbf{k}^S - \mathbf{k}^I = \pm\mathbf{q} \tag{15a}$$

$$\omega^S - \omega^I = \pm\omega_\alpha(\mathbf{q}). \tag{15b}$$

In the above equations, the plus sign stands for the so called anti-Stokes events, when a phonon is annihilated in the process and the scattered photon is more energetic having gained energy from the medium, while the minus sign corresponds to the so-called Stokes events, when a new phonon is created in the process and the scattered photon is less energetic having transferred energy to the medium. In the classical wave picture, the second equation represents the Doppler shift of an electromagnetic wave *dynamically diffracted* by an elastic wave moving either in the direction of vector $\mathbf{q}$ or in the direction of vector $-\mathbf{q}$ with the same absolute sound velocity. To see how Brillouin inelastic scattering may be viewed as a Bragg reflection of the incident wave, let us consider eq. energy with the aid of the dispersion relations for photons $\omega^I = c|\mathbf{k}^I|$ and $\omega^S = c|\mathbf{k}^S|$ and phonons:

$$\frac{|\mathbf{k}^S| - |\mathbf{k}^I|}{|\mathbf{q}|} = \frac{v_\alpha}{c}.$$

The order of magnitude of the ratio v_α/c could be typically 10^{-5} so that $|\mathbf{k}^S| \approx |\mathbf{k}^I|$. Because the energy of a photon is $c\hbar|\mathbf{k}|$ the scattering is quasi-elastic. Taking this into account and squaring eq. momentum one easily obtains:

$$2|\mathbf{k}^I|\sin(\varphi/2) = |\mathbf{q}|$$

where φ is the scattering angle. The above equation can be given the form of Bragg law $2d\sin(\theta) = \lambda$, being $\theta = \varphi/2$ the Bragg angle. The grating spacing d is equal to the phonon wavelength $2\pi/|\mathbf{q}| = 2\pi v_\alpha/\omega_\alpha|$ and $\lambda = \lambda_\circ/n$ is the wavelength of the incident photon in the medium, while $\lambda_\circ$ is the corresponding quantity in vacuum. From the above considerations, it turns out that the measurement of the Brillouin shift $\Delta\omega = |\omega^S - \omega^I| = \omega_\alpha$ in a fixed scattering geometry (e.g. backscattering with $\varphi = \pi$) leads to the possibility of measuring the sound velocity v_α, provided the index of refraction of the medium n is known, by means of the formula:

$$v_\alpha = \frac{\lambda_\circ|\Delta\omega|}{4\pi n\sin(\varphi/2)}. \tag{16}$$

Most Brillouin scattering experiments reported in this review paper were done using a backscattering geometry ($\boldsymbol{k}^S = -\boldsymbol{k}^I$) unless when explicitly signaled. The equations of conservation of wavevector and energy are only necessary conditions for the scattering events to take place. To have a complete information one must compute the intensity of the scattered wave, or the *elasto-optic* scattering cross section. Once this is done, particular selection rules appear in connection with the scattering angle, the polarizations of both photons and phonons and their relative orientations with respect to the scattering plane (defined by the vectors $\mathbf{k}^I$ and $\mathbf{k}^S$); moreover, in the case of crystalline bodies, the dependence of v_α on the phonon propagation direction (elastic anisotropy) must be taken into account.

In the following, we shall restrict ourselves to the case of optically isotropic solids. The key ingredient of bulk Brillouin scattering theory is the instantaneous anisotropic dielectric susceptibility of the medium around the frequency ω^I, the tensor

$$\chi_{ij}(\mathbf{r}, t) = \chi\delta_{ij} + \delta\chi_{ij}(\mathbf{r}, t) \tag{17}$$

χ is the usual time-independent isotropic susceptibility, while the tensor $\delta\chi_{ij}(\mathbf{r}, t)$ is the anisotropic fluctuating part of the susceptibility due to the presence of thermal phonons. Then, the fluctuating part of the *polarization vector* radiating the scattered waves can be written as $\delta P_i = \varepsilon_\circ\delta\chi_{ij}E_j$, $\varepsilon_\circ$ being the vacuum dielectric constant. Here, $E_j = E_j^I + E_j^S$ is the sum of the incident field and of the scattered field. Using the linearity of Maxwell equations, the scattered electric field $\mathbf{E}^S$ can now be computed by means of first-order perturbation theory (Born approximation [16]):

$$\delta P_i \approx \varepsilon_0 \delta\chi_{ij} E_j^I \tag{18}$$

The above equation is justified by the smallness of both the scattered field and $\delta\chi_{ij}$. In fact, the coupling between sound and light (the *elasto-optic effect*) can be written in terms of two elasto-optic constants a_1 and a_2 as

$$\varepsilon_0 \delta\chi_{ij} \;=\; a_1 e_{ij} \;+\; a_2 \varepsilon_{ll} \delta_{ij} \tag{19}$$

and the phonon strains ε_{ij} are very small.[2] Sometimes a_1 and a_2 are written in terms of the Pockels coefficients p_{ij} as $a_1 = -\varepsilon^2(p_{11} - p_{12})$ and $a_2 = -\varepsilon^2 p_{12}$ [3,15]. For a cubic crystal three independent coefficients are necessary to express the elasto-optic coupling. In equation radiation, δP_i oscillates at the frequency $\omega^S \;= \omega^I \;\pm \omega_\alpha(\mathbf{q})$ because E_j^I is proportional to $e^{i\omega^I t}$ and $\delta\chi_{ij}$, being proportional to the strain field of a bulk phonon oscillates as its normal coordinate $\xi_{\boldsymbol{\alpha}}(\mathbf{q}) = Q_{\mathbf{q}\boldsymbol{\alpha}} e^{\pm i\omega_\alpha(\mathbf{q})t}$ does. Solving the radiation problem (the Maxwell's equations with a source proportional to $\partial(\delta P_i)/\partial t$ [16]), the scattered electric field can be obtained. Once this is known the spectral intensity of the scattered light is computed as the power spectrum $S_{E^s}(\omega)$ which is essentially the measured outcome of a Brillouin scattering experiment:

$$S_{E^s}(\omega) \;=\; \int_{-\infty}^{\infty} < E^S(t+\tau) E^{S*}(t) >_{th} e^{i\omega\tau} d\tau \tag{20}$$

where $E^S = \mathbf{E}^S \cdot \mathbf{e}^S$ is the complex amplitude of the scattered field projected along a given analyzed polarization direction $\mathbf{e}^S$ perpendicular to $\mathbf{k}^S$. An explicit computation gives [17]:

$$S_{E^s}(\mathbf{Q},\omega,) \propto \frac{\left|E_0^I\right|^2}{\lambda_0^4} \left|\mathbf{e}^S \cdot \delta\boldsymbol{\chi}_{\mathbf{Q}} \bullet \mathbf{e}^I\right|^2 < |\xi_\alpha(\mathbf{q})|^2 >_{th} \delta\left[\omega - (\omega^I + \omega_\alpha(\mathbf{q}))\right] \tag{21}$$

for anti-Stokes scattering. For Stokes scattering one has just to replace $\omega^I + \omega_\alpha(\mathbf{q})$ with $\omega^I - \omega_\alpha(\mathbf{q})$ in the argument of the delta function. In the classical limit, valid for Brillouin scattering, $< |\xi_\alpha(\mathbf{q})|^2 >_{th} \propto k_B T/\omega_\alpha^2(\mathbf{q})$. In all practical applications, the delta function is substituted by a Lorentzian lineshape centered at $\omega^I \pm \omega_\alpha(\mathbf{q})$ (*Brillouin doublet*) with an FWHM related to the *lifetime* of the phonon and to *instrumental* and *opacity* broadening [15]. $\mathbf{e}^I$ is the polarization of the incident electric field. In Equation (21)

$$\delta\boldsymbol{\chi}_{\mathbf{Q}} = \int_V \delta\boldsymbol{\chi}(\mathbf{r}') e^{-i\mathbf{Q}\cdot\,\mathbf{r}'} d\mathbf{r}' \tag{22}$$

is the Fourier transform of index **Q** of the spatial part of the susceptibility tensor fluctuation, the *transferred wavevector* **Q** being defined as

$$\mathbf{Q} = \mathbf{k}^S - \mathbf{k}^I.$$

Because the bulk phonon *wavefunction* is a plane wave $\propto e^{i\mathbf{q}\cdot\mathbf{r}}$, computing $\delta\chi_{\mathbf{Q}}$ we get:

$$\delta\chi_{\mathbf{Q}} \propto \int_V e^{-i(\mathbf{Q}-\mathbf{q})\cdot\mathbf{r}'} d\mathbf{r}' \propto \delta(\mathbf{Q}-\mathbf{q}) \tag{23}$$

that is, the wavevector conservation momentum. The fact that **Q** must be equal to the phonon wavevector **q** to have a peak in the spectrum is typical of Brillouin scattering by bulk phonons in transparent materials. The partial relaxation of this rule in the case surface waves and/or of opaque media is one of the most characteristic points in the theory of surface Brillouin scattering [15]. The main results that can be obtained from a detailed analysis of eqs. intensity, Fourier and Pockels, can be summarized as follows: (a) the light scattered by transverse phonons is completely depolarized; (b) there is no scattering by transverse phonons polarized in the scattering plane; (c) the intensity of scattering from transverse phonons goes to zero in back scattering; (d) scattering by longitudinal phonons is fully polarized, that is keeps the polarization of the incident wave.

In case of volume Brillouin scattering from a liquid, a phenomenology similar to that of solids can be found, where the traveling diffraction grating responsible for the scattering process is made by longitudinal acoustic modes. The main differences with respect to solids are that: (*i*) transverse modes cannot propagate in the liquid – at least for frequencies lower than that of the structural relaxation – and (*ii*) longitudinal acoustic modes, i.e. collective density fluctuations, are affected by non-negligible attenuation processes. In this condition, the isotropic part of the Brilliouin spectrum is proportional to that of density fluctuations $\delta\rho(\boldsymbol{q},t)$ [18]. In the case of simple homogeneous liquids, the linearized hydrodynamic equations, neglecting the thermal diffusion mode, and its contribution to the acoustic damping, give the equation of motion of density fluctuations [19]:

$$\left[\left(\frac{\rho}{q^2}\right)\frac{\partial^2}{\partial t^2} + \eta_l\frac{\partial}{\partial t} + M\right]\delta\rho(q,t) = 0 \tag{24}$$

where ρ is the static mass density, $M = \rho v_l^2$ is the adiabatic longitudinal modulus, v_l the adiabatic sound velocity, and η_l the static longitudinal viscosity, responsible for the damping of acoustic waves.

Looking for harmonic solutions, $\delta\rho \propto \exp(i\omega t)$, the presence of a complex elastic modulus $\tilde{M}(\omega) = M + i\omega\eta_l$ becomes apparent in Equation (24). It is interesting to notice that this simple viscoelastic model, appropriate for simple liquids, corresponds to the low frequency limit ($\omega T_\varepsilon << 1$) of the Zener model, provided that

$\eta_l = \left(M_U - M_R\right)\tau_\varepsilon$. The power spectrum of density fluctuations, directly obtained from the Equation (24) is that of a damped harmonic oscillator (DHO):

$$I(\omega) = \frac{I_0}{\pi} \frac{\Gamma_b \omega_b^2}{\left(\omega^2 - \omega_b^2\right)^2 + \left(\Gamma_b \omega\right)^2} \tag{25}$$

where ω_b and Γ_b approximately correspond to the frequency position and full width at half maximum of the Brillouin peaks, respectively. Also in case of more sophisticated models for the complex elastic modulus [20], the DHO equation can be used to fit Brillouin spectra from viscoelastic materials, provided that a narrow frequency region around the Brillouin peak is analyzed and apparent, ω-dependent, values of $M(\omega_b)$ and $\eta(\omega_b)$ are defined. The DHO parameters are related to $M(\omega_b)$ and $\eta(\omega_b)$ through: $M(\omega_{b)} = \rho\omega_b^2/q^2$, and $\eta(\omega_{b)} = \rho\Gamma_b/q^2$.

Surface Brillouin scattering

Surface Brillouin Scattering (SBS) became a practical spectroscopic technique more than 40 years ago grace to the great progress made in Fabry Perot interferometry by John Sandercock (for a review see [15]). Because the formal theory of surface Brillouin scattering is rather complex and usually involves cumbersome computations both of the phonon density of states and of the scattering cross section [14], we shall outline here qualitatively only the main characteristic conclusions that can be drawn from Equation (22). First of all the finite penetration depth of light in the material (e.g. about 1000 nm in Si and only a few nm in Al at $\lambda_\circ$= 514 nm, the typical wavelength of an Argon Laser) profoundly modifies the wavevector conservation law momentum.

Being δ the skin depth of the light, the effective scattering volume is limited in the direction z perpendicular to the surface within a length of the order of δ that can be less than the light wavelength $\lambda \approx |n\mathbf{k}^I|^{-1}$. We then define a complex transferred wavevector $\mathbf{Q} = Q_{||}\hat{\mathbf{e}}_x + (Q_\perp - i\delta^{-1})\hat{\mathbf{e}}_z$ to be used in eq. Fourier. Moreover, taking into account that the *phonon wavefunction* of a true surface wave is proportional to $e^{iq_{||}x}\sum_n b_n e^{-\kappa_{\alpha n}z}$, with κ_α of the same magnitude as $q_{||}$, from Equation (22) it is found that

$$\delta\chi_{\mathbf{Q}} \propto \delta(Q_{||} - q_{||}) \sum_n \frac{b_n}{\kappa_{\alpha n} + \delta^{-1} + iQ_\perp}. \tag{26}$$

Due to the absence of $q_{\perp n}$ in the imaginary part of the denominator, only parallel wavevector conservation can occur even in the case of very low opacity. Introducing θ_i as the incidence angle and θ_s as the angle (positive in the clockwise direction) between the outgoing surface normal and the scattering direction and considering that $Q_{||} = \pm\, q_{||}$, we find

$$|\mathbf{k}^I|(\sin\theta_s - \sin\theta_i) = \pm q_{||}, \tag{27}$$

which is the fundamental kinematic relation of SBS. In backscattering, as $\theta_s = -\theta_i$, we obtain

$$\omega_{n\alpha} = v_{n\alpha}\frac{4\pi}{\lambda_0}\sin\theta_i \tag{28}$$

where $\omega_{n\alpha}$ is the Brillouin shift of a surface peak, $v_{n\alpha}$ is the phase velocity of the surface phonon responsible for the SBS event and $q_{||} = (4\pi/\lambda_0)\sin\theta_i$ is the allowed wavevector. Then, in backscattering, the SBS peak shifts of non dispersive SAWs (e.g. the Rayleigh wave) scale as the sine of the incidence angle, while the volume BS peak shifts of bulk phonons (eq. shift) do not depend on the angle. If the subsurface structure is not homogeneous but layered the surface waves are dispersive and $v_{n\alpha} = v_{n\alpha}(q_{||})$ in a non-trivial way for each different type of surface phonon [14]. The measurement of the dispersion relations is an effective way to measure the elastic constants of the surface once the density is known. The elasto-optic coupling is not the only SBS channel. A second *scattering mechanism*, the *ripple effect* can be operative if the phonons have a shear vertical polarization component [15]. In fact these phonons modulate the instantaneous shape of the free surface. The dynamically corrugated surface, depending on its reflectivity, scatters the incident light and, due to Doppler effect, there appear scattered photons with frequencies shifted from ω^I. It turns out that the ripple scattering cross section is proportional to the power spectrum of the u_z displacement field computed at the surface ($z = 0$) and, thus, to $g_{SV}(\omega q_{||}|0)$, the SV *surface projected phonon density of states* [14,17].

Brillouin scattering from parallel to the surface modes

Parallel-to-the-surface (PS) modes, appear in the Brillouin spectrum of thin films deposited on flat surfaces for thicknesses higher than few micrometers as an hybridization of Sezawa modes (the so called longitudinal guided modes), eventually developing into pure bulk acoustic modes traveling parallel to the surface. Revealing bulk phonons through this scattering geometry gives the opportunity to obtain the velocity of acoustic modes from the frequency of Brillouin peaks through Equation (28), without the need of an independent evaluation of the refractive index, which is required in the traditional volume Brillouin scattering (see below, Par. *Brillouin Spectroscopy from biomaterials*)

Brillouin scattering of nanostructured films

In inhomogeneous *low-density, low-dimensional, and disordered materials*, the crossover between confinement and propagation of acoustic phonons strongly influences the possibility of using Brillouin scattering to characterize the materials and has a profound basic interest too. Though promising theoretical models do exist for the analysis of some complex inhomogeneous materials [29], in the absence of a clear and widely accepted theory, the matter is discussed on the basis of experimental findings only. Moreover, the possibility of measuring the *local* mechanical properties of these materials at the mesoscale by Brillouin scattering is critically discussed.

Cluster-assembled materials

Nano-structured cluster-assembled materials are thoroughly described in refs. [21–26]. Experimental characterization and theoretical modeling of such materials have to face the problem of cluster coalescence and of their organization in structures spanning length scales from the nanometer up to the micrometer. The different structures in which the precursor clusters are organized need experimental probes sensitive to the different length scales typical of intra-cluster and inter-cluster interactions. For carbon-based materials, as we have already discussed, Raman spectroscopy can be used for a characterization on a nanometer scale [17,32]. In order to study the organization of clusters on a scale of hundreds of nanometers, which is the typical scale of thermally excited long wavelength acoustic phonons, Brillouin light scattering was used for the first time by Bottani et al. [27]. Films of graphite, polycrystalline diamond, diamond-like a-*C:H*, C_{60} (fullerite), and phototransformed C_{60} have also been studied by Brillouin scattering [17]. Normally, SBS is applied to homogeneous compact films with perfect (atomically flat) surfaces and buried interfaces [14]. Particularly challenging is instead the attempt of getting and interpreting Brillouin spectra of films with a rough surface and/or a granular or porous structure. The extraction of the elastic properties of these systems from the spectroscopic data can be based only partially on what is known in the case of *good* films and a complete theory is still lacking [29]. Bulk and surface Brillouin scattering signals have been obtained from films characterized by a complex structure from the atomic to the hundreds of nanometers level, showing that this technique can be used also for nano-structured materials with irregular surfaces. Bulk and shear modulus of the material have been determined giving information on the acoustic properties on a mesoscopic scale. This allows to infer the nature of the bonding between the carbon aggregates.

Thick films (thickness ≥ 1 µm) and thin films (down to thickness ≅ 20 *nm*) have been examined. The results depend strongly on the presence (or the absence) of a beam focalizer selecting (or not) only clusters of small size during the supersonic cluster beam deposition (SCBD) process [25].

Films grown by an unfocused beam

In thick films ($d > 2\pi/q_{||}$) only damped bulk acoustic phonons with a typical wavelength λ_{ph} of the order of 170 *nm* have been detected. This indicates that for a length $d \geq \lambda_{ph}$ the film bulk can be modeled as a continuum with approximate translational invariance and effective elastic constants although structural disorder at smaller scales scatters the phonons significantly. The presence of a rather strong central peak in the spectra could be ascribed to non-propagating (overdamped), or confined vibrational excitations, probably connected with different characteristic correlation lengths less than *d*. The most damped bulk acoustic phonons could be coupled to the confined modes by a relaxation mechanism. The surface phonons could be almost overdamped if not already replaced by surface fractons or by localized cluster modes. Instead in thinner films, notwithstanding the high degree of surface roughness, which increases with film thickness, intense surface Rayleigh wave peaks can be detected up to a critical thickness of the order of 200 *nm* (Figure 1 top). To make the SBS spectrum measurable the films must be grown on an ultrasmooth high reflecting substrate to maximize the buried interface ripple scattering [29]

Films grown by a focused beam

Films with a completely different nanostructure, more compact and with smoother surface, can be grown using the focalization device. Typical spectra of focalized films are shown in Figure 1 bottom. The study of a thick film with respect to a thin films gives an advantage: we can consider the film as a semi-infinite medium and so the nature and the characteristics of the acoustic waves propagating in the system are not affected by the thickness (often not known with enough accuracy), and thus by the presence of the substrate.

These spectra are interesting mainly for the high intensity and small width of the Rayleigh peak, never observed before in cluster-assembled carbon films. This feature supports the conclusion that long life acoustic phonons can propagate along the film surface, in other words at a mesoscopic scale of observation this film appears as a homogeneous elastic continuum and the relatively low surface roughness, acting as surface structural disorder, introduces only a small acoustic damping factor without hindering the phonon propagation (as in the case of non-focalized films). This fact is consistent with a smooth surface film of compact material made of close-packed small clusters and it is important in comparison with the results of BS experiments on the deposited without beam focalization in which the surface roughness increases as the film thickness. Measuring the dispersion relations of the surface phonons the elastic constants of the films can be estimated. The best results are obtained for the Young modulus E as demonstrated by a detailed sensitivity analysis [28]. Using for the density ρ values coming from X-ray reflectivity [14] (all values are in the range 1–1.3 g cm^{-3}) the found elastic constants are, typically, of the order: $C_{11} = 5.4$ GPa, $C_{44} = \mu = 2.5$ GPa, $E = 4.6$ GPa, $B = 1.9$ GPa, and $\nu = 0.1$. These values are comparable to those obtained from the thin films (thickness of about 100 nm or less) deposited with unfocused beam [29], in particular they are near to the values of the harder of this thin film series. The comparison with diamond elastic constants indicates a very soft and highly deformable material with a shear modulus (for shear between graphene planes) near to that of graphite. These results can be compared with Raman measurements [17] which point out the mainly sp^2 carbon bonding present in the disordered granular structure of the films on a nanometer scale (see Figure 2). Yet the film material is not elastically identical to nanocrystalline graphite: in fact the values of B (and, consequently, v) are significantly different. Similar problems are discussed in [33].

Elastic surface wave anomalies near the cluster-to-layer transition of Au on NaCl

In quasi-2D cluster systems surface Brillouin scattering can show the percolation threshold from cluster to film regimes through the detection of acoustic anomalies of surface waves [30]. In this paper, it was reported for the first time on investigations of elastic surface wave excitations near the cluster-to-layer transition of Au on NaC1(001) by means or Brillouin scattering. A softening in the dispersion of the first-order localized Sezawa mode with decreasing layer thickness indicates the transition from a continuous to a discontinuous or island layer. In the cluster regime a new type or acoustic surface mode is observed at frequencies above the transverse acoustic (TA) phonon frequency of the substrate. The crossing or this new cluster mode with the TA phonon frequency coincides with the percolation threshold as evidenced by electron micrographs.

Propagating and confined acoustic modes in crystalline polymer latex films

More recently, the percolation threshold has been detected by surface Brillouin scattering during the sintering process of crystalline polymer latex particles [31]. Structural evolution of polytetrafluoroethylene latex polymer films has been studied by Brillouin light scattering and atomic force microscopy (AFM). Using a tunable sintering process, the authors have controlled the degree of particle connectivity yielding a crossover in the behavior of acoustic excitations ranging from confined modes to propagating phonons. This transition has been correlated also to the surface morphology by AFM (Figure 3). Fully sintered films are characterized by extended “fibrillar” crystalline regions embedded in a disordered matrix, which still retain features of the original particulate structure.

Brillouin spectroscopy from biomaterials

While Raman spectroscopy is already recognized as powerful tool in the biomaterials characterization [34,35], only in the last years BLS has clearly demonstrated extreme effectiveness in this field.[36–39].

Understanding mechanical properties of heterogeneous biomaterials is an important challenge, since they depend on the properties of the single components, their structural arrangement and mutual interaction. The experimental investigation of the viscoelastic properties of biomaterial can be performed at different length and time scales, giving complementary information on their static and dynamic properties. In this frame, Brillouin spectroscopy is progressively emerging as non-contact, non-invasive, and label-free technique, which is ideal for measuring sound velocity and attenuation in the micrometer/10-picosecond spatial/temporal scale. Some case studies are reviewed in the following, which help to understand the potential of BLS applied to biomaterials.

One of the earliest biological applications of Brillouin spectroscopy date back to 1977, when it was used to determine the elastic moduli of ***collagen*** obtained from rat rail tendon, and to try estimating the hydrogen bond force constants and the association of water with collagen in the native state [40]. The study was later extended to include measurements of anisotropy of the elastic constants of collagen, revealing both longitudinal and transverse acoustic waves traveling at different angles to the fiber axis. [41] More recently, a detailed BLS investigation of the mechanical properties of elastin and collagen fibers has been realized by means of an innovative interaction geometry, with samples placed on a reflective substrate to reveal both bulk phonons and parallel to surface (PS) longitudinal and transverse modes (see Figure 4) [37,42].

This geometry allowed to investigate the dependence of the BLS spectrum on fiber orientation, required to fully characterize the elasticity tensor with five independent components, typical of a hexagonally symmetric elastic medium. Elastic constants were combined to give axial and transverse Young's, shear and bulk moduli of the fibers. These were 10.2, 8.3, 3.2 and 10.9 GPa, and 6.1, 5.3, 1.9 and 8 GPa for dehydrated-type I collagen and elastin, respectively.

The moduli of collagen and elastin are much higher than those measured at lower frequency using macroscopic strains, and the difference between them is much less, suggesting molecular-scale viscoelastic effects, as described in Par. [*Time dependence: anelastic relaxation*], to be responsible for the frequency dependence of the fiber biomechanics.

The same scattering geometry used for the BLS characterization of collagene (thin flat sample over a reflective substrate) was also used for the determination of the mechanical properties of ***bone matrix***, and compared with results obtained by nanoindentation and scanning acoustic microscopy [43]. It was shown that, though BLS requires longer acquisition times with respect to the other techniques, it is unique in allowing an easy measure of the in-plane anisotropy of wave velocities for both logitudinal and transverse phonons.

The existence of hierarchical structures in biological matter at the micrometer level can give strong nonlinear strain-dependent behavior to phonons in the GHz range. An interesting case is that of longitudinal phonons revealed by BLS on ***spider dragline silk*** [44]. Spider silk is a remarkable natural fiber, possessing an unmatched combination of reversible extensibility and high tensile strength. BLS was used to reveal acoustic phonons propagating at different directions along the fibers and estimate the first-order mechanical response, which consists of five independent elastic constants. However, spider silk possesses highly nonlinear, anisotropic, viscoelastic behavior which means that the measured phonon frequencies are altered when it is mechanically deformed, hampering efforts to extract the purely linear elastic contribution. More recently, BLS investigation of spider dragonlike silk has revealed the presence of a hypersonic phononic bandgap and of a negatively dispersive region. These features have been attributed to the interplay between the uniaxial symmetry of the nanofibrils and non-local nonlinear mechanical behavior of the surrounding inhomogeneous amorphous polymer matrix [45].

Another successfull field of application of BLS to biological samples is the measure of elastic properties of ***lens and cornea of the eye***. The first BLS investigation of eyes was performed in 1980 by a traditional setup [46]. More recently, this field has been revitalized by the development of micro-Brillouin imaging, as described below.

Brillouin micro-spectroscopy

The first realization of imaging of mechanical properties of a sample by BLS was proposed in 2005 from a solid–liquid interface with 20-μm spatial resolution [47]. Two years later, the first application of confocal Brillouin spectroscopy was proposed for the 3D imaging of an intraocular lens and of the crystalline lens in a mouse eye [38]. The most relevant novelty introduced by that work was the use of virtually imaged phase array (VIPA) spectrometers, which was able to reduce the acquisition time for a single spectrum to fractions of second. This improvement fostered a fast increase of interest toward the use of micro BLS for the mechanical mapping of biological and biomedical samples [48], extending its applicability to *in vivo* diagnosis [49,50]. An overview of the progress up to 2015 can be found in Ref. [51]. In more recent years, the research and development activity has been focused on improving the performances of the interferometers, in order to enlarge the field of application of micro-Brillouin, specially toward biomedical fields. Spatial resolution has reached sub-cellular dimensions (see Figure 5), so that 3D ***imaging of single cells*** is now possible, resolving internal structures of single cells [52]. Increasing spatial resolution was possible thanks to the use of high numerical aperture lenses, taking properly into account the induced broadening of Brillouin peaks [65,66].

The opacity of biological samples and the non-negligible intensity of light back-reflected by the optics in the back-scattering geometry requires the use of ***high contrast interferometers*** to discriminate the low intensity of Brillouin peaks over the intense leakage of elastic light signal. To this aim, a continuous effort has been devoted to develop high contrast interferometers by use of, e.g.

multi-stage setups [53], molecular absorption cells [54], destructive interference [55], or by equalizing the interfering transmitted field components [56]. A new multi-pass Fabry–Perot interferometer has been also recently proposed, with a contrast higher than 150 dB, for back-scattering Brillouin measurements in very opaque and reflective samples [57]. Complex and structured biological samples can now be investigated by Brillouin micro-spectroscopy, such as microbial biofilms [58,59], tumoral tissues [60], and cellular nuclei [61].

One of the most promising routes for the development of micro-Brillouin spectroscopy is that of ***correlative measurements***, where different optical and/or spectroscopic mapping techniques are developed to operate in parallel, at the same time and in the same volume analyzed by Brillouin spectroscopy. To this respect, the co-detection of fluorescence and BLS signals has been demonstrated as a powerful tool to study, e.g. mechanotransduction and intracellular signaling pathways of plant extracellular matrices [62].

Correlative Brillouin–Raman micro-spectroscopy

Recently, an innovative micro-spectrometer has been realized, able to simultaneously collect Raman and Brillouin signals from the same scattering volume [57]. Brillouin–Raman micro-spectroscopy (BRMS) allows to perform correlative studies, comparing viscoelastic and chemical properties, which can be simultaneously mapped with sub-micrometer resolution on the same sample. A schematic of the setup is reported in Figure 6. Its potential has been already established in microbiology [57,59], tissues characterization [60,63,64], and cellular biomedical applications [51,65].

Interesting results have been obtained by analizing chemo-mechanical maps of ***Candida biofilms*** [57,59]. Biofilms are almost ubiquitous aggregates of microbes growing onto solid surfaces, embedded into a eso-polysaccharides (EPS) matrix, with an increased resistance to antibiotics, anti-fungal drugs, and extreme conditions. The mechanical characteristics of the biofilm, are related to stability and dispersion of cells involved in the biofilm. BRMS allowed to identify two main softening mechanisms of dried biofilms, one due to a high concentration of EPS, and the other to the presence of residual water [59].

The combination of reduced stiffness (Figure 7(f)) and increased acoustic attenuation (Figure 7(h)) observed in the central region of the linear scan in Figure 7 has been attributed to the plasticizing effect associated to an increase of residual water. In fact, both spectral changes can be attributed to a reduction of the structural relaxation time, i.e. of local viscosity, associated with a local increase in hydration level. At the same time, in the same place, Raman–Brillouin spectra confirm the presence of water with an order of magnitude increase of the OH peak (Figure 7(c)) and suggest a factor three higher thickness (three microbial layers) for the increase of intensity of CH (Figure 7(e)) and Brillouin (Figure 7(d)) peaks. These results (larger thickness, more plastic behavior, more intense

Raman signals) can be interpreted in terms of a volume inside the biofilm where a chemico-physical condition is preserved that is more favorable to the survival of Candida cells. This is also confirmed by the large increase of Raman signals in the 1510–1750 cm^{-1} region (Figure 7(g)) that can be, at least partially, attributed to the resonant scattering from cytochrome c, a marker of cell vitality. This case study shows that BRMS is able to reveal what is not visible in the optical image: a region of higher thickness, where the buried cells have been protected by the overlaying biofilm structure, preserving water and vitality of the inner cells.

BRMS has been also succesfully applied to the mechanical mapping with chemical specificity of biomedical samples, such as Barrett's oesophagus [60,63] and amyloid plaques. [64] ***Barrett's oesophagus*** is a condition characterized by a change in the lining of the esophagus that markedly increases the risk of adenocarcinoma. The site-matched application of Brillouin microscopy, Raman microscopy and FTIR micro-spectroscopic imaging to ex-vivo epithelial tissue – Barrett's oesophagus [60,63] reported elasticity maps of the epithelium, correlated with 'chemical images'. Evidence of hydrated (type I) collagen fibrils forming the extracellular matrix and of embedded epithelial cells was provided by Raman scattering spectra at gland/connective tissue interface. Micro-Brillouin mapping of the glandular region showed signatures of high scattering intensity in correspondence of low-frequency shift and higher acoustic attenuation, a viscoelastic effect that was attributed to higher hydration of collagen fibrils.

Strong viscoelastic changes have been also evidenced in correlative Brillouin–Raman mapping of amyloid plaques in the hippocampal part of the brain of a β-amyloid overexpressing transgenic mouse [64]. The plaque core has shown high rigidity, identified by a marked increase in Brillouin peak frequency, associated with the abnormal deposition of β-amyloid protein, which is a typical pathological hallmark of ***Alzheimer's disease*** (see Figure 8). The surrounding tissue presents high viscoelasticity in correspondence of a lipid-rich layer (evidenced by Raman spectra) around the dense core of the plaque and high heterogeneity in the external tissue, plausibly due to the presence of cell bodies (i.e. astrocytes and microglia).

In general, these results demonstrated that BRMS maps are very sensitive to changes in tissues at a cellular level and is therefore a valuable tool for histological analysis, with potential for *in vivo* diagnosis of pathology.

BRMS has been recently proposed for studying mechanical properties correlated with biochemical composition of ***living fibroblasts under physiological conditions*** [65]. Single living cells immersed in their buffer solution have been mapped, revealing the mechanical heterogeneities inside the cell. The area of the Raman amide 1 peak and the proteins versus lipids ratio, which can both be considered as spectroscopic measures of the protein concentration, appear strictly correlated with the cell elasticity, confirming the key role of protein structures in conferring rigidity to the cell. Moreover, by analyzing the DNA Raman signal vesus the elastic modulus, the nucleus if found to occupy the stiffer cell zone, with a 20% increase in the elastic modulus passing from the plasmatic membrane to the nucleus. Brillouin line shape analysis is even more relevant for the comparison of cells under physiological and pathological conditions. Following oncogene expression, cells show an overall reduction in the elastic modulus (15%) and apparent viscosity (50%), which can be explained by a general modification of the cytoskeletal properties assigned to the deregulation of protein expression. In this regard, the invasive potential of cancer cells is clearly correlated to the modification of their mechanical properties, favoring their diffusion into tissues. The ability of BRMS to follow the spatial and eventual temporal modulations of cellular mechanical properties, which are intimately related to physiological or pathological processes, strongly support the future application of this technique for fundamental issues in the biomedical field.

Notes

1. Strictly speaking, the term phonon should be reserved to crystalline bodies owning microscopic discrete translational invariance. Here, we use the same term in the hydrodynamic limit even for amorphous bodies.
2. $e_{ik} = \varepsilon_{ik} - \frac{1}{3}\delta_{ik}\varepsilon_{ll}$ is a pure shear strain (a *strain deviator*, where δ_{ik} is the unit tensor): in fact $e_{ll} = 0$, proving e_{ik} is a pure shear.

Disclosure statement

No potential conflict of interest was reported by the authors.

Funding

This work was supported by the ENSURE: European Research Council (ERC) under the European Union's Horizon 2020 research and innovation programme [grant number 647554].

ORCID

Carlo E. Bottani http://orcid.org/0000-0002-2015-7043

References

[1] G.A.D. Briggs (ed.), *Advances in Acoustic Microscopy*, Vol. 1, Plenum Press, New York, 1995.
[2] C. Kittel, *Introduction to Solid State Physics*, 3rd ed., John Wiley & Sons, New York, 1966.
[3] L.D. Landau and Lifshitz, *Theory of Elasticity*, 2nd ed., Pergamon Press, London, 1970.
[4] J.D. Achenbach, *Wave Propagation in Elastic Solids*, Elsevier, North Holland, Amsterdam, 1990.
[5] A.S. Nowick and B.S. Berry, *Anelastic relaxation in crystalline solids*, Academic Press, New York, 1972.
[6] N.G. McCrum, B.E. Read and G. Williams, *Anelastic and Dielectric Effects in Polimeric Solids*, Dover Publications, New York, 1991.
[7] J.D. Ferry, *Viscoelastic properties of polymers*, 2nd ed., Wiley-Interscience, New York, 1970.

[8] G.P. Srivastava, *The physics of phonons*, Adam Hilger, Bristol, PA, New York, 1990.

[9] C.E. Bottani, G. Ghislotti and P. Mutti, J. Phys.: Condens. Matter 6 (1994) p.L85.

[10] G. Ghislotti and C.E. Bottani, Phys. Rev. B 50(12) (1994) p.131.

[11] C.E. Bottani and R. Caporali, J. Phys.:Condensed Matter 6 (1994) p.L791.

[12] R. Caporali, C.E. Bottani and G. Ghislotti, Phys. Rev. B 53 (1996) p.4133.

[13] G.W. Farnell and E.L. Adler, *Elastic wave propagation*, in *Thin Layers in Physical Acoustics* vol. 9, P.W. Mason and R.W. Thurston, eds., Academic Press, New York, 1972, p.35.

[14] M. Beghi, C.E. Bottani, P.M. Ossi, T. Lafford and B.K. Tanner. J. Appl. Phys. 81 (1997) p.672;G. Carlotti, Appl. Sci. 8 (2018) p.124 (a review paper);T. Wittkowsky, J. Jorzick, K. Jung and B. Hillebrands, Thin Solid Films 353 (1999) p.137;P. Djemia, F. Ganot, P. Moch, V. Branger and P. Goudeau, J. Appl. Phys. (2001) p.90, 756;G. Carlotti, D. Fioretto, G. Socino, B. Rodmacq and V. Pelosin, J. Appl. Phys. (1992) 71 p.4897.

[15] Sandercock J.R., *Trends in Brillouin light scattering: studies of opaque materials, supported films and central modes*, in Light Scattering in Solids III, M Cardona and G. Güntherodt, eds., Springer Verlag, Berlin, 1982, p.173.

[16] Born M. and Wolf E., Principles of Optics (VII exp. ed.), Chapter XII, Cambridge University Press, Cambridge, 1999.

[17] P. Milani and C.E. Bottani, Vibrational spectroscopy of Mesoscopic Structures, in *Handbook of Nanostructured Materials and Nanotechnology* Vol. 2, H.S. Nalwa, ed., Academic Press, New York, NY, 2000, p.213;G. Carlotti, D. Fioretto, G. Socino, B. Rodmacq and V. Pelosin, J. Appl. Phys. 71 (1992) p.4897.

[18] B.J. Berne and R. Pecora, *Dynamic Light Scattering*, John Wiley & sons, New York, 1976.

[19] L. Comez, D. Fioretto, F. Scarponi and G. Monaco, J. Chem. Phys. 119 (2003) p.6032.

[20] L. Comez, C. Masciovecchio, G. Monaco and D. Fioretto, Solid State Physics 63 (2012) p.1.

[21] M.M.J. Treacy, T.W. Ebbesen and J.M. Gibson, Nature 381 (1996) p.678.

[22] G.A.J. Amaratunga, M. Chowalla, C.J. Kiely, I. Alexandrou, R. Aharonov and R.M. Devenish, Nature 383 (1996) p.321.

[23] J.P. Lu, Phys. Rev. Lett. 79 (1997) p.1297.

[24] P. Melinon, V. Paillard, V. Dupuis, A. Perez, P. Jensen, A. Hoareau, J.P. Perez, J. Tuaillon, M. Broyer, J.L. Vialle, M. Pellarin, B. Baguenard and J. Lerme, Int. J. Mod. Phys. B 9 (1995) p.339.

[25] P. Milani and S. Iannotta, *Cluster Beam Synthesis of Nano-structured Materials*, Springer Verlag, Berlin, 1999.

[26] M.S. Dresselhaus, G. Dresselhaus and P.C. Eklund, *Science of Fullerenes and Carbon Nanotubes*, Academic Press, San Diego, CA, 1996.

[27] C.E. Bottani, A.C. Ferrari, A. Li Bassi, P. Milani and P. Piseri, Europhysics Lett. 42 (1998) p.431.

[28] R. Pastorelli, S. Tarantola, M.G. Beghi, C.E. Bottani and A. Saltelli, Surf. Sci. 468 (2000) p.37.

[29] B.R. Braeckman, P. Djemia, F.T. Tard, L. Belliard and D. Depla, Surfacd Coat. Technol. 475 (2017) p.483; C.S. Casari, A. Li Bassi, C.E. Bottani, E. Barborini, P. Piseri, A. Podestà and P. Milani, Phys. Rev. B. 64 (2001) p. 0854171.

[30] B. Hillebrands, R. Mock and G. Güntherodt, Solid State Commun. 60 (1986) p.649.

[31] M. Pierno, C.S. Casari, R. Piazza and C.E. Bottani, Appl. Phys. Lett. 82 (2003) p.1532.

[32] L. Ravagnan, F. Siviero, C. Lenardi, P. Piseri, E. Barborini, P. Milani, C.S. Casari, A. Li Bassi and C.E. Bottani, Phys. Rev. Lett. 89 (2002) p.285506.

[33] D. Dellasega, V. Russo, A. Pezzoli, C. Conti, N. Lecis, E. Besozzi, M. Beghi, C.E. Bottani and M. Passoni, Mater. Des. 134 (2017) p.35–43.

[34] H.J. Butler, L. Ashton, B. Bird, G. Cinque, K. Curtis, J. Dorney, K. Esmonde-White, N.J. Fullwood, B. Gardner, P.L. MartinHirsch, M.J. Walsh, M.R. McAinsh, N. Stone and F.L. Martin, Nat. Protoc. 11 (2016) p.664–687.

[35] K. Kong, C. Kendall, N. Stone and I. Notingher, Adv. Drug Delivery Rev. 89 (2015) p.121.

[36] K. Elsayad, S. Werner, M. Gallemí, J. Kong, E.R. Sánchez Guajardo, L. Zhang, Y. Jaillais, T. Greb and Y. Belkhadir (2016) Sci. Signal. **9,** rs5.

[37] F. Palombo, C. Peter Winlove, R.S. Edginton, E. Green, N. Stone, S. Caponi, M. Madami and D. Fioretto, J. R. Soc. Interface 11 (2014) p.20140739.

[38] G. Scarcelli and S.H. Yun, Nat. Photonics 2 (2007) p.39.

[39] G. Antonacci and S. Braakman, Sci. Rep. 6 (2016) p.37217.

[40] R. Harley, D. Lames, A. Miller and J.W. White, Nature 267 (1977) p.285.

[41] S. Cusack and A. Miller, J. Mol. Biol. 135 (1979) p.39.

[42] R.S. Edginton, S. Mattana, S. Caponi, D. Fioretto, E. Green and C.P. Winlove, J. Vis. Exp. 115 (2016) p.e54648 doi:https://doi.org/10.3791/54648.

[43] M. Matsukawa, R. Tsubota, M. Kawabe and K. Fukui, Ultrasonics 54 (2014) p.1155.

[44] K.J. Koski, P. Akhenblit, K. McKiernan and J.L. Yarger, Nat. Mater. 12 (2013) p.262.

[45] D. Schneider, N. Gomopoulos, C.Y. Koh, P. Papadopoulos, F. Kremer, E.L. Thomas and G. Fytas, Nat. Mater. 15 (2016) p.1079.

[46] J.M. Vaughan and J.T. Randall, Nature 284 (1980) p.489.

[47] K.J. Koski and J.L. Yarger, Appl. Phys. Lett. 87 (2005) p.061903.

[48] G. Antonacci, R.M. Pedrigi, A. Kondiboyina, V.V. Mehta, R. de Silva, C. Paterson, R. Krams and P. Török, J. R. Soc. Interface 12 (2015) p.20150843.

[49] G. Scarcelli, P. Kim and S.H. Yun, Biophys. J. 101 (2011) p.1539.

[50] G. Scarcelli, S. Besner, R. Pineda, P. Kalout and S.H. Yun, JAMA Ophthalmol. 133 (2015) p.480.

[51] Z. Meng, A.J. Traverso, C.W. Ballmann, M.A. Troyanova-Wood and V.V. Yakovlev, Adv. Opt. Photonics 8 (2016) p.300.

[52] G. Scarcelli, W.J. Polacheck, H.T. Nia, K. Patel, A.J. Grodzinsky, R.D. Kamm and S.H. Yun, Nat. Methods 12 (2015) p.1132.

[53] G. Scarcelli and S.H. Yun, Opt. Express 19 (2011) p.10913.

[54] Z. Meng, A.J. Traverso and V.V. Yakovlev, Opt. Express 22 (2014) p.5410.

[55] G. Antonacci, G. Lepert, C. Paterson and P. Török, Appl. Phys. Lett. 107 (2015) p.061102.

[56] G. Antonacci, S. De Panfilis, G. Di Domenico, E. DelRe and G. Ruocco, Phys. Rev. Appl. 6 (2016) p.054020.

[57] F. Scarponi, S. Mattana, S. Corezzi, S. Caponi, L. Comez, P. Sassi, A. Morresi, M. Paolantoni, L. Urbanelli, C. Emiliani, L. Roscini, L. Corte, G. Cardinali, F. Palombo, J.R. Sandercock and D. Fioretto, Phys. Rev. X, 7 (2017) p.31015.

[58] A. Karampatzakis, C.Z. Song, L.P. Allsopp, A. Filloux, S.A. Rice, Y. Cohen, T. Wohland and P. Török, npj Biofilms Microbiomes 3 (2017) p.20.

[59] S. Mattana, M. Alunni Cardinali, S. Caponi, D. Casagrande Pierantoni, L. Corte, L. Roscini, G. Cardinali and D. Fioretto, Biophys. Chem. 229 (2017) p.123.

[60] F. Palombo, M. Madami, D. Fioretto, J. Nallala, H. Barr, A. David and N. Stone, J. Biophotonics 9 (2016) p.694.

[61] J. Zhang, X.A. Nou, H. Kim and G. Scarcelli, Lab Chip 17 (2017) p.663.

[62] K. Elsayad, S. Werner, M. Gallemi, J. Kong, E. R. Sanchez Guajardo, L. Zhang, Y. Jaillais, T. Greb and Y Belkhadir, *Sci. Signaling* 9 (2016) p. rs5.

[63] F. Palombo, M. Madami, N. Stone and D. Fioretto, The Analyst 139 (2014) p.729.

[64] S. Mattana, S. Caponi, F. Tamagnini, D. Fioretto and F. Palombo, J. Innovative Opt. Health Sci. 23 (2017) p.1742001.

[65] S. Mattana, M. Mattarelli, L. Urbanelli, K. Sagini, C. Emiliani, M. Dalla Serra, D. Fioretto and S. Caponi, Light Sci. Appl. 7 (2018) p.e17139.

[66] G. Antonacci, M.R. Foreman, C. Paterson and P. Török, Appl. Phys. Lett. 103 (2013) p.221105.